Nonlinearities and carrier dynamics in refractory plasmonic TiN thin films

HEATHER GEORGE,[1] JENNIFER REED,[2] MANUEL FERDINANDUS,[3] CLAYTON DEVAULT,[4] ALEXEI LAGUTCHEV,[6] AUGUSTINE URBAS,[2] THEODORE B. NORRIS,[1] VLADIMIR. M. SHALAEV,[5] ALEXANDRA BOLTASSEVA,[5] AND NATHANIEL KINSEY[5,7,*]

[1]*Electrical Engineering, University of Michigan, Ann Arbor MI 48109, USA*
[2]*Air Force Research Laboratory, Wright-Patterson Air Force Base, OH 45433, USA*
[3]*Air Force Institute of Technology, Wright Patterson AFB, OH 45433, USA*
[4]*School of Physics and Astronomy, Purdue University, West Lafayette IN 47907, USA*
[5]*School of Electrical and Computer Engineering, Purdue University, West Lafayette IN 47907, USA*
[6]*Birck Nanotechnology Center, Purdue University, West Lafayette IN 47907, USA*
[7]*Now at Department of Electrical and Computer Engineering, Virginia Commonwealth University, Richmond VA 23284, USA*
[*]*nkinsey@vcu.edu*

Abstract: Titanium nitride is widely used in plasmonic applications, due to its robustness and optical properties which resemble those of gold. Despite this interest, the nonlinear properties have only recently begun to be investigated. In this work, beam deflection and non-degenerate femtosecond pump-probe spectroscopy (800 nm pump and 650 nm probe) were used to measure the real and imaginary transient nonlinear response of 30-nm-thick TiN films on sapphire and fused silica in the metallic region governed by Fermi-smearing nonlinearities. In contrast to other metals, it is found that TiN exhibits non-instantaneous positive refraction and reverse saturable absorption whose relaxation is dominated by slow thermal diffusion into the substrate lasting several hundred picoseconds. Ultrafast contributions arising from hot-electron excitations are found to be a small part of the overall response, only appearing significant in the TiN on fused silica at irradiance levels above 100 GW-cm^{-2}. The modeling and origin of this response is discussed, and TiN is found to be adept at achieving ultrafast (below 1 ps) lattice heating which, combined with the robustness and low-cost of the material may prove useful in various thermo-optical applications such as local heating, heat-assisted processes, and nanoscale heat transfer.

1. Introduction

The study of nonlinear optical processes has been a hotbed for photonics research since the invention of the laser, leading to the development of numerous technologically important devices and systems for wavelength conversion, ultrafast control, and optical characterization [1,2]. Although the nonlinear optical properties of metals have also been studied for many years, there has been a recent renewal of interest in metals due to their plasmonic properties and ability to confine light down to subwavelength dimensions [3–5]. For example, both propagating and local surface plasmons are extremely sensitive to changes in the complex permittivity of the metallic layer and the surrounding environment, facilitating numerous applications in low-intensity optical sensing or all-optical signal control [6–8]. Alternatively, plasmonic components can be used to effectively confine light to extremely tight volumes where locally enhanced fields can result in increased nonlinearities for polymers, quantum wells, glasses, or other dielectric nonlinear materials [9–12]. However, the development of such devices has been limited by the softness

of traditional plasmonic materials, melting point depression for nanostructures, and film creep [13,14].

Recently, the development of alternative plasmonic materials has provided several candidates that possess optical properties mimicking those of gold but are able to withstand temperatures in excess of 2800 °C before melting. These so-called refractory plasmonic materials [14–17], e.g. TiN, ZrN, HfN, and TaN, may provide a good solution for applications such as nonlinear plasmonics [18], photothermal cancer therapy [19,20], water treatment [21], nanoparticle trapping [22,23], or local chemical reaction control [24,25]. Recent works using a metal-insulator-metal configuration have demonstrated hot-electron detectors with TiN exhibiting an order of magnitude greater photocurrent than a similar device using Au [26,27]. Furthermore, TiN shows a greater heating efficiency when compared to gold over most of the visible and near infrared spectrum [28], useful for thermo-photovoltaic applications [14]. In nonlinear optics, metal films have been shown to produce a large nonlinear index change [2,29] and facilitate harmonic generation [30]. More recently, the plasmonic effects of metals have been utilized to localize electric fields and provide enhancement to other nonlinear materials such as polymers and quantum wells. However the softness of many traditional metals remains a limitation under large optical intensities, and the robustness of TiN combined with respectable plasmonic performance makes the material a leading candidate [14]. Due to this interest, studies in TiN has demonstrated nonlinear frequency conversion [17,31] while other efforts have studied the degenerate effective third-order nonlinear optical properties of TiN thin films [32] although the temporal response of the effect is just beginning to be studied for thick films and oxy-nitride layers [33,34].

In this work, we combine non-degenerate transient pump-probe and beam deflection experiments to study the strength of the nonlinearities, their temporal dependence, and their origin. We find that the response in TiN films under our experimental conditions exhibits a positive refraction and reverse saturable absorption effect, dominated by a large (90% of signal) decay lasting several hundred picoseconds, while exhibiting a weak (10%) ultrafast contribution. This is in stark contrast to many other metallic films (e.g. gold, silver) which exhibit negative refraction and saturable absorption with strong ultrafast (<10 ps) nonlinear transients. Utilizing a dual-parabolic two-step model to identify both the electron and lattice temperature decays, we compare the origins of these effects to the most optically similar material, gold.
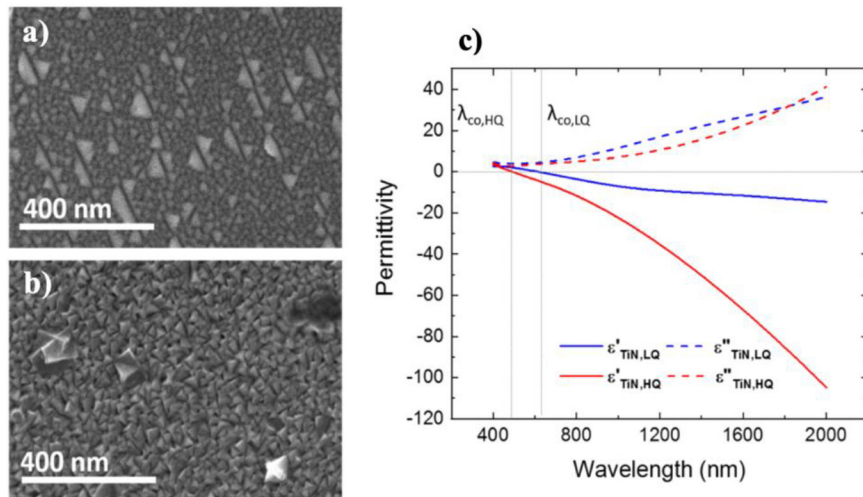

Fig. 1. a) SEM image of the high-quality TiN surface illustrating a smooth, well-ordered cubic grains. b) SEM image of the low-quality TiN surface illustrating randomly oriented cubic grains. Linear permittivity of the TiN samples.

2. Results

2.1. Titanium nitride samples

Two 30 nm thick TiN samples were studied in this work, a film grown at 800 °C on c-sapphire and a film grown at 350 °C on fused silica (see Appendix A). To illustrate the differences between the samples, the surface structure of the TiN was imaged via scanning electron microscope. For the sapphire-based film, referred to as the "high-quality sample", a smooth surface with well-ordered grains is found, which is expected for a textured epitaxial film (see Fig. 1a) [35,36]. Conversely, for the fused silica-based film, referred to as the "low-quality sample", a randomized grain orientation is observed, which a consequence of polycrystalline nature of the sample (see Fig. 1(b)).
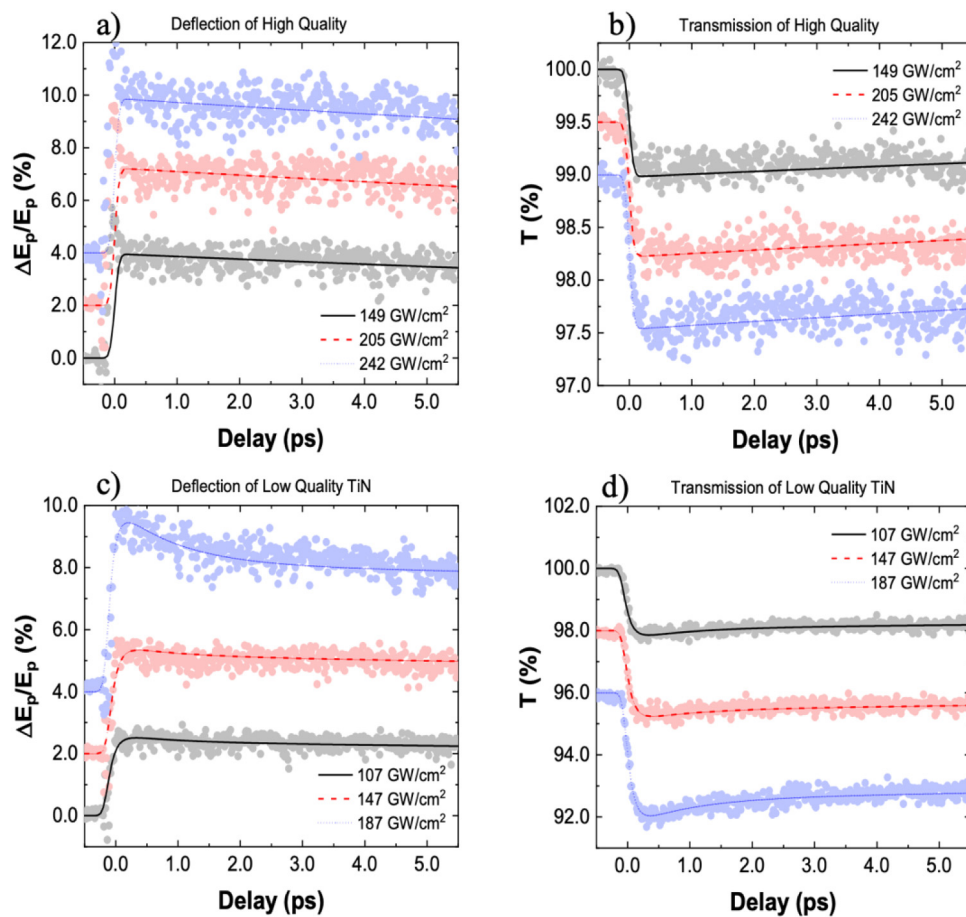
2.2. Optical measurements

Fig. 2. Beam deflection measurements of the a) beam displacement and b) total power transmitted for high-quality TiN on fused sapphire at 800° C and the measurements of the c) beam displacement and d) total power transmitted for low-quality TiN on fused silica at 350° C. Note that the red and blue signal traces are shifted (2% in panels a, c, d and 0.5% in b) in order to facilitate visibility. Circles represent experimental data and solid lines represent numerical fitting. Pump excitation is centered at time zero.

To study the nonlinearities in TiN, we use a combination of the beam deflection method [37] and time-resolved differential transmission (TRDT). Beam deflection provides a powerful method for determining the amplitude of the nonlinear response, while the TRDT measurements enable direct comparison of the hot electron dynamics with that of traditional metal films, which has a substantial literature. The beam deflection measurements were performed using a Ti:sapphire laser operating at a 1 kHz repetition rate where the pump pulse was set to 800 nm (~40 fs) and the probe pulse was set to 650 nm (110 fs) with parallel polarization (see Appendix B.1. for details). The results of the beam deflection measurements for the two TiN samples are shown in Fig. 2 and a summary of the extracted nonlinear coefficients is shown in Table 1, obtained using the procedure as described by M. Ferdinandus et al. [38], (further details provided in Appendix B.2.). Considering these results, two key points are readily apparent: 1) the samples exhibit positive nonlinear refraction and reverse saturable absorption; 2) the response of both films is dominated by a slow relaxation mechanism lasting much longer than 5 ps although a small ultrafast (< 2 ps) contribution is observed in the low-quality film, Figs. 2(c) and 2(d). These two observations stand in contrast to other metallic films, such as gold [29,39,40], which exhibit a Fermi-smearing nonlinear effect in their metallic regions due to free-carrier absorption, giving rise to a strong ultrafast transient with negative refraction and saturable absorption [41]. We do note in the high-quality film deflection, Fig. 2(a), a sharp peak near time zero is observed only in the deflection measurement. Although this feature is repeatable, its temporal width is limited by the pump-probe cross-correlation and is strongly reduced under cross-polarized experiments, suggesting an ultrafast effect that is likely a residual signal from the substrate.

Table 1. Nonlinear Coefficients from Beam Deflection

	Mechanism 1			Mechanism 2		
Sample	$n_{2,\text{eff}}$ [m²-W⁻¹]	α_2 [m-W⁻¹]	τ_f [ps]	$n_{2,\text{eff}}$ [m²-W⁻¹]	α_2 [m-W⁻¹]	τ_r [ps]
High-Quality TiN	-	-	-	4.7×10^{-13}	2.15×10^{-7}	38.0
Low-Quality TiN	2.2×10^{-15}	2.8×10^{-9}	1	8.5×10^{-13}	1.3×10^{-6}	97.4

Extracted nonlinear coefficients, $n_{2,\text{eff}}$, α_2 and characteristic times, for the two TiN films under test where mechanism 1 represents an ultrafast transient while mechanism 2 represents a long-lived response. Definitions of the nonlinear coefficients are taken as described in [57] and detailed in appendix.

To observe the transient on longer time scales, a TRDT experiment was used as this technique is less sensitive to small pump-probe alignment deviations, which occur over long delay stage travel distances. In this setup, the pump wavelength was again set to 800 nm (~150 fs) and the probe to 650 nm (~200 fs) with a repetition rate of 250 kHz. The relative transmission change of the two films is shown in Fig. 3 for short and long-time scales, where the transmission results from beam deflection have been overlaid for comparison. The TRDT response at early times matches well with the transmission results of beam deflection and the response of the samples appear similar. However, on a longer time scale the difference between the samples becomes more apparent, although both samples exhibit a measurable residual transmission for times beyond 1 ns.

2.3. Experimental analysis

To identify the origins of the decay dynamics in the TiN samples, we consider that at both the pump (800 nm) and probe (650 nm) wavelengths, the dominant optical absorption mechanism is free-carrier absorption, as both wavelengths are well below the valence-to-conduction band transition energy (~5-7 eV) [42,43]. In this case, we might expect the absorption of pump photons to produce hot electrons that relax on the order of a few picoseconds. In normal metals this behavior is typically described with a two-temperature model (TTM) [44–48] where the lattice temperature is usually not seen as playing a role within this initial time frame and is used
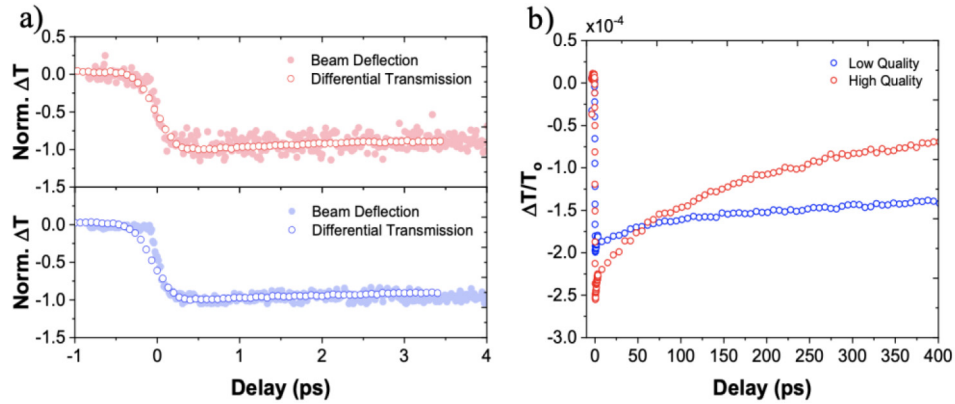
Fig. 3. a) Comparison of the normalized beam deflection and time-resolved differential transmission (TRDT) measurements for the high-quality sample (red) and low-quality sample (blue) on a short time scale, showing excellent agreement. Data was normalized by dividing by the absolute value of the peak change in transmission. b) Change in transmission over long time scales using TRDT. All data in panel a) were normalized.

to explain a small long-lived offset in TRDT data. However, this assumption relies on two key points: 1) the temperature change of the electron population is much larger than the lattice ($T_{film} \approx T_e$) in the temporal region of interest and 2) the rise time of the lattice temperature is long compared to the pulse width such that there are two clear relaxation regimes, see example for gold in Fig. 7 [47–49]. TiN's response is clearly quite different.

The abrupt change is followed by a slow relaxation feature extending for 100's of ps. In contrast to the behavior of gold, in TiN fast and slow contributions appear to be much more closely intertwined. This indicates that the lattice temperature, typically seen to produce merely a small offset, is significantly contributing to the optical response. This was verified by finite element simulations of the thermal decay in the TiN films, where an excellent match to the decay beyond 10 ps was found for both films assuming constant TiN thermal properties and varying thermal properties for the sapphire and fused silica substrates (details presented in Appendix D For times less than 10 ps, hot-electron effects are not considered in the simulation and can lead to a deviation in the response.

Under these conditions, the standard TTM would not be sufficient to model the TiN films as a decay of the lattice temperature must be included. An adequate description can be achieved by moving to a Dual-Parabolic Two-Step (DPTS) model [50,51]:

$$C_e(T_e)\frac{\partial T_e}{\partial t} = \nabla[\kappa_e \ \nabla T_e] - G(T_e - T_l) + S(z,t) \tag{1}$$

$$C_l(T_l)\frac{\partial T_l}{\partial t} = \nabla[\kappa_l \ \nabla T_l] + G(T_e - T_l) \tag{2}$$

which includes the lattice relaxation, and allows the overall temperature of the film to be represented as a linear combination of the lattice and electron temperatures ($\Delta T = A\Delta T_e + B\Delta T_l$) [44,52]. More information on this model can be found in Appendix D. To support the model, the electron-phonon coupling coefficient (G) was estimated to be on the order of 10^{18} W-K^{-1}-m^{-3} using the approximation introduced by Allen, et al. [53] and constants from literature (Appendix C Using the DPTS and allowing the G parameter to vary, reasonably accurate fits with the entire high-quality TiN experimental data set can be obtained (Fig. 4), taking G $\approx 0.7\times10^{17}$ W-K^{-1}-m^{-3} which is approximately 2-orders of magnitude larger than gold [54]. Using similar fitting parameters, the model was also able to qualitatively fit the low-quality TiN films save for a

constant mismatch in the temperature relaxation at long times. This offset is believed to be due to the thermal conductivity of the low-quality TiN that differs from the bulk, and/or a poor interface conductance between the TiN/fused silica which is not present in the case of the more ideal TiN on sapphire [55]. Improved fitting and modelling may be accomplished with more accurate measurement of the fundamental properties of as-grown TiN films.
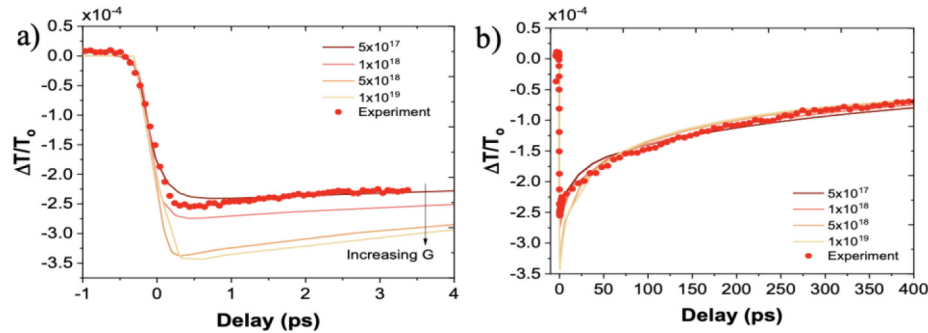

Fig. 4. Time-resolved differential transmission measurements for the high-quality film modeled using the parabolic two step approach over a) the short time window and b) the long-time window for different values of G. G is listed in units of $W\text{-}K^{-1}\text{-}m^{-3}$.

3. Discussion

Using the DPTS model, we can isolate the role of the hot-electron and lattice temperatures on the nonlinear response. As a reference, we calculate the response of gold using values from literature in Fig. 5, producing a response dominated by the hot-electron decay (see Appendix D.2).
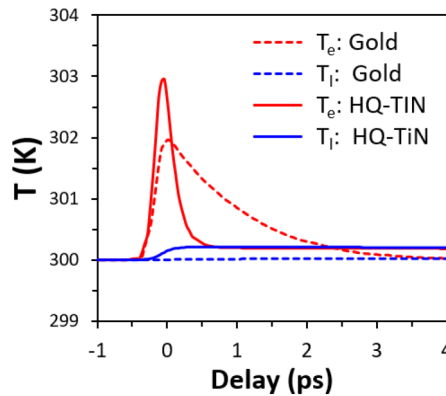

Fig. 5. The temperature rise in gold (dashed lines) and the high-quality (HQ) TiN (solid lines) for a 6 $\mu J\text{-}cm^{-2}$ pump pulse.

Similarly, the high-quality TiN exhibits the typical rise in both electron and lattice temperatures, yet they equilibrate in less than one picosecond with a lattice temperature rise that is 6× larger than in gold. The quick hot-electron decay can be attributed to a G parameter that is approximately 2 orders of magnitude larger than in gold [54], while the rise in the TiN lattice temperature can be attributed to 3× more absorption, decreased reflectivity of the material and larger loss, combined with a thermal conductivity that is an order of magnitude less. As a result, the slow thermal decay is expected to be a much larger portion of the overall signal, and in our case is found to produce a response comparable to the hot-electron response. Alternatively, in the low-quality

sample, the reduced carrier density produces an electron heat capacity that is ~2× lower than in the high-quality sample, thereby producing a larger change in the refractive index for a given optical irradiance (see Table 1). As a result, the ultrafast hot-electron response is found to be more evident, especially at large irradiances, although the overall response is still found to be dominated by the slow lattice decay.

It is important to note that unlike in gold and other high thermal conductivity films, the overall transient response is not expected to be significantly altered by varying the thickness of the film on insulating substrates. As the thermal properties of sapphire and TiN are extremely similar, and the interface is known to have a good thermal conductance [55], this sample can approximate the response of a bulk TiN slab. As a result, the slow relaxation should be carefully taken into account when considering plasmonic applications of TiN.

4.   Conclusion

The nonlinear optical response of plasmonic refractory TiN thin films were studied using a combination of the beam-deflection method and TRDT. TiN films interrogated with a non-degenerate pump at 800 nm and probe at 650 nm are observed to have positive nonlinear refraction, reverse saturable absorption, a fast hot-electron decay, and a response dominated by a prolonged lattice thermal relaxation. Although atypical for conductive metallic films, this combination of behaviors is particularly useful in two key application areas: 1) local heating, 2) nonlinear enhancement. For applications in local heating, such as photothermal cancer therapy, water treatment, nanoparticle trapping, or local chemical reaction control, the rapid and efficient transfer of energy from the electrons to the lattice is beneficial to produce a nearly instant rise in the temperature and allows a higher peak value to be achieved. For nonlinear enhancement, the primary goal of the metallic component is to localize the electric field to drive a nearby nonlinear material whose response is typically ultrafast (e.g. electronic polarization). When the metallic component itself has an ultrafast effect, the response can pollute the overall signal, and the lack of any such effect in TiN may be beneficial as it decouples the design of the plasmonic resonator and nonlinear response. Furthermore, the large damage threshold of TiN and high melting temperature, even when nanostructured, ensure that operation in harsh environments and under peak irradiance levels exceeding 200 GW-cm^{-2} (55 fs) are possible. As a result, refractory TiN is an especially promising material for thermo-plasmonic applications including those utilizing intense ultrafast laser pulses.

Appendix A: TiN growth and linear characterization

The TiN films were fabricated using DC reactive magnetron sputtering in an argon/nitrogen environment with 4 sccm of Ar and 6 sccm of N$_2$ at a deposition pressure of 5 mTorr. A 30 nm thick TiN film was deposited on a 0.7 mm thick fused silica substrate at a low substrate temperature of 350°C. A second 30 nm thick film was also deposited on a 0.5 mm thick sapphire substrate at a high substrate temperature of 800°C.

Table 2. Summary of the Drude-Lorentz model parameters used to fit the spectroscopic ellipsometry data for the two TiN films.

Sample	ε_∞	A$_{Drude}$ [eV^2]	B$_{Drude}$ [eV]	A$_1$ [eV^2]	B$_1$ [eV]	E$_1$ [eV]	A$_2$ [eV^2]	B$_2$ [eV]	E$_2$ [eV]
High-Quality TiN	5.2	49.2	0.2	5.7	1.6	2.0	24.1	1.0	3.5
Low-Quality TiN	3.3	25.6	0.8	4.5	0.9	1.0	39.5	2.5	3.5

The linear optical properties of both samples were studied using variable angle spectroscopic ellipsometry and subsequent fitting with a Drude-Lorentz model in a manner similar to previous reports [56]. The fitting parameters are shown in Table 2.

Appendix B: Beam deflection measurement

B.1. Experimental set-up

Beam deflection measurements are performed as described by M. Ferdinandus et al. [37,38], using a Ti:sapphire amplified system (KM Labs Wyvern 10-1000) producing 4.2 mJ, 55 fs (FWHM) pulses at 800 nm operating at a 1 kHz repetition rate. The strong excitation pulse is obtained by splitting ~5 µJ of the fundamental with a beam splitter. An optical parametric generator/amplifier (Light Conversion TOPAS-Prime) is pumped by the fundamental to generate the 650 nm (second harmonic of signal), 110 fs probe pulse, which is then spatially filtered to produce a Gaussian irradiance profile. The probe is focused to a spot size, w_p, ~3-5× smaller than that of the excitation, w_e, both of which are determined by knife-edge scans. The probe is displaced from the peak of the excitation to the maximized irradiance gradient at $(1/2)w_e$ where the probe experiences an induced refractive index, Δn, gradient, causing it to be deflected by a small angle, $d\Phi$. The maximum index gradient is found by shifting the excitation until the maximum deflection signal is achieved at zero temporal delay. The deflection signal is measured using a quad-segmented Si photodiode (OSI QD50-0-SD) which simultaneously measures the differential signal (ΔE) and the total signal (E_o), each of which is detected by a lock-in amplifier (Stanford Systems SR-830). A mechanical optical chopper (ThorLabs MC-2000) synchronized with the excitation repetition rate is used to modulate the excitation at 286 Hz.

Since the TiN samples are on either silicon dioxide or sapphire substrates, the nonlinear response of these materials must be removed from the measurement in order to isolate the effect of the TiN film alone. To do so the samples were half coated with TiN while the other half was left uncoated. First the coated half was measured, then the sample was translated laterally so that the bare substrate could be measured without a realignment of the experimental system. The signal from the substrate is then removed from the TiN raw data after being scaled based on the transmissivity of the TiN. Small artifacts can remain in the signal if the substrate is not highly uniform or if translating the sample causes it to move slightly in-line with the beam. These artifacts will appear as peaks centered roughly at time zero which are limited by the cross correlation of the pump and probe temporal profiles, indicating that they are due to an instantaneous nonlinear response and not from the TiN film.

B.2. Determination of nonlinear coefficients

The nonlinear coefficients are defined as in the paper by M. Reichert et al [57] where the total index change resulting from multiple nonlinear optical response mechanisms is given by $\Delta n = n_{2,el}I[t] + \int_{-\infty}^{\infty} R[t - t']I[t']dt'$ where the first term is the index change from the electronic nonlinear index $n_{2,el}$ and $I[t]$ is temporal profile of the irradiance. The second term is the index change from the various non-instantaneous responses and is the convolution of the sum of temporal response functions $R[t]$ and $I[t]$. $R[t] = \sum_m n_{2,m}r_m[t]$ where $n_{2,m}$ the coefficient associated with a particular response function m and $r[t]$ is the temporal profile of the nonlinear response normalized so that $\int_{-\infty}^{\infty} r_m[t]dt = 1$. For the case of TiN, the non-instantaneous decays were modeled as a biexponential function $r[t] = C \left(1 - Exp\left[-\frac{t}{\tau_r}\right]\right) Exp\left[-\frac{t}{\tau_f}\right] \Theta[t]$ where C is the normalization factor, τ_r is the rise time, τ_f is the fall time and $\Theta[t]$ is the Heaviside function to ensure causality. In this case, the instantaneous electronic nonlinearity was set to zero during the fitting as this feature was not observed in the TiN data.

Because the decay times are very long for this material, the normalization factor C ends up being very small, which hence requires that n_2 for these mechanisms be very large. Therefore, the magnitudes of n_2 for the various mechanisms range over several orders of magnitude, and accounts for the wide range of magnitudes of the electronic and free-carrier nonlinearities.

Appendix C: Estimation of electron-phonon coupling coefficient

Given the long-lasting thermal relaxation, we can determine that TiN possess either an extremely weak electron phonon coupling such that hot-electrons are long lived, or that the coupling is extremely fast such that the lattice is heated on a timescale similar to the pulse width which then relaxes slowly. To determine the correct approach, the electron-phonon coupling coefficient (G) was determined from constants reported in literature using the approximation introduced by Allen, et al. [53]:

$$G = \frac{3\gamma\lambda \ \langle\omega^2\rangle}{\hbar\pi k_B} \tag{3}$$

where γ is the electron constant for the heat capacity, and λ is the Bardeen-Cooper-Schrieffer electron phonon coupling constant from superconductor theory, and ω^2 is the second moment of the phonon spectrum, which can be estimated as $\omega^2 \simeq (\Theta_\infty)^2$ [58]. Though these equations were derived for superconductors, such as TiN, they have been successfully used to estimate the G parameter at room temperature for non-superconductors such as gold, and the results have been found to agree with measured values [52]. Subsequently, using values for TiN found in literature (Table 3) an electron-phonon coupling coefficient on the order of 10^{18} W-K^{-1}-m^{-3} is predicted, illustrating that hot-electrons are short-lived in TiN and the lattice heats quickly.

Table 3. TiN Constants from Literature

Constant	Value	Reference
γ [mJ-mol^{-1}-K^{-2}]	2.5–3.6	[58,59]
λ	0.59–0.64	[60–63]
Θ_∞ [K] [a]	487–518	[63]
$\langle\omega^2\rangle$ [J^2] [b]	4.5×10^{-41}˜5.1×10^{-41}	calculated
G [W-K^{-1}-m^{-3}]	3.6×10^{18} – 6.5×10^{18}	calculated

The second moment is calculated from the Debye values

Appendix D: Simulations

D.1 COMSOL simulations

To confirm the role of the lattice temperature, simulations of the thermal decay in TiN films on the fused silica and sapphire substrates were completed using the finite element method (COMSOL Multiphysics). An impulse injection of heat to the TiN lattice was taken at zero time, thereby modelling an instantaneous transfer of optical energy from the heated Fermi-sea to the TiN (i.e. $G \rightarrow \infty$). To compare the simulation with experiments we assume a constant thermal index coefficient $\frac{d\tilde{n}}{dT}$, such that the change in transmission is proportional to the change in temperature. The simulation was configured to be 2-D axially symmetric with a 30 nm thick layer of TiN on top of a 1 μm thick substrate. Both layers were considered to have a radius of 200 μm. The central axis boundary condition was axial symmetry, while the bottom of the substrate and outer edge of the sample were fixed to room temperature 293 K. The top surface of the TiN layer was set to allow a heat flux. The energy ($Q_{in}(r,z)$) deposited into the TiN layer was calculated based on the energy absorbed within the TiN considering an incident Gaussian beam of width 50 μm. The TiN was then set to have an initial temperature $T_{in}(r,z) = Q_{in}(r,z)/(C_p\rho V)$, where ρ is the density and V is the illuminated volume. The thermal and optical properties of the materials is listed in Table 4. The temperature of the TiN layer is taken from a point at r = 0 precisely halfway into the thickness of the TiN, and the temperature at this point in time is extracted.
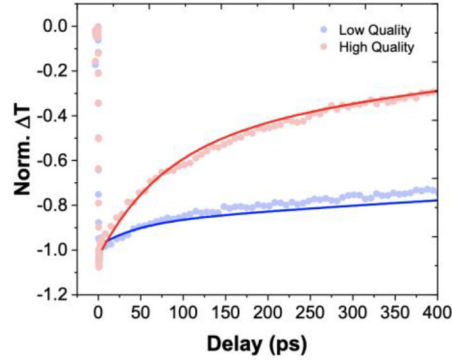
Fig. 6. Normalized lattice temperature as obtained from simulation, solid lines, (which is proportional to the change in sample transmission) overlaid with the normalized experimental transmission data, data points, versus time. This demonstrates that for times beyond 10 ps the response is described by heat transfer between the TiN film and substrate. The experimental data was normalized by dividing by the change in transmission at 10 ps (approximate time where COMSOL becomes a valid estimate) while simulation was normalized by dividing by peak rise in temperature. The simulation data was then inverted for comparison with experimental data.

Table 4. Summary of Material Properties used in the Finite Element Simulations

Material	κ [W-m^{-1}-K^{-1}]	C_p [J-kg^{-1}-K^{-1}]	ρ [kg-m^{-3}]	α [m^{-1}]
TiN LQ	28	602	5210	3.76×10^7 *
TiN HQ	28	602	5210	5.48×10^7 *
Fused Silica	1	680	2650	-
Sapphire	25	880	3690	-

All values were taken from [65,66], except * values which were determined from experiments and the heat capacity of TiN which was determined from [67].

The resulting temperature decay for the TiN samples are shown in Fig. 6, where an excellent agreement is observed, confirming that the slow relaxation time in TiN is due to a thermal index change, not a hot-electron decay. This conclusion is also supported by recent measurements of the temperature dependent index in TiN films [64], where a positive $\frac{d\text{Re}\{\tilde{n}\}}{dT}$ due to the thermal expansion of the unit cell volume and a subsequent reduction in the free-electron density along with a positive $\frac{d\text{Im}\{\tilde{n}\}}{dT}$ due to increased phonon scattering is observed. As a result, the relaxation time is limited by the rate of thermal dissipation and can be impacted by varying the thermal properties of the TiN-substrate interface, the substrate conductivities of the substrate, the TiN-substrate interface, and the thickness of the TiN layer.

D.2 Dual-parabolic two-step model

TiN exhibits a strong lattice contribution which is not well-described by the standard TTM. To improve the capture of this response, the Dual-Parabolic Two-Step model [50,51] was used:

$$C_e(T_e)\frac{\partial T_e}{\partial t} = \nabla[\kappa_e \ \nabla T_e] - G(T_e - T_l) + S(z,t) \tag{4}$$

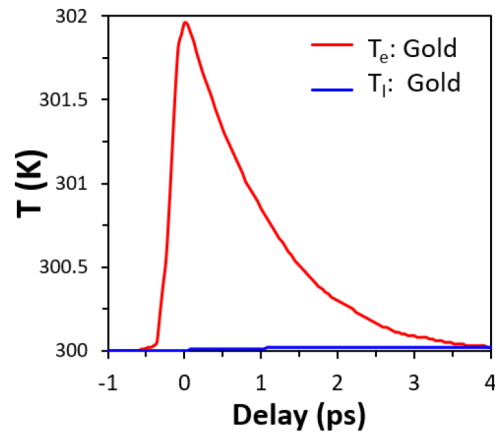$$C_l(T_l)\frac{\partial T_l}{\partial t} = \nabla[\kappa_l \ \nabla T_l] + G(T_e - T_l) \tag{5}$$

Fig. 7. Electron and lattice temperatures of a thin gold film following a 6 μJ-cm^{-2} optical pump at time zero, illustrating a typical ultrafast decay due to hot-electrons and long-lived offset due to lattice heating.

In the traditional heat equation, the thermal conductivity is just a single value in one equation; however, when trying to separate out the contributions from the electrons and the lattice, the electrons provide the thermal conductivity and the lattice contributes < 1%. In our model, $\kappa_l = 0.0005 \; \kappa_{\text{bulk}}$. C_e is a temperature dependent variable which has different equations for different temperature regimes, however, this work stays in the linear regime:

$$C_e = \gamma T_e \tag{6}$$

where γ, [J-m^{-3}-K^{-2}] is the electron contribution to the heat capacity.

Table 5. Summary of the Material Properties used in the Numerical Calculations

Material	κ [W-m^{-1}-K^{-1}]	C_e [J-m^{-3}-K^{-1}]	C_l [J-m^{-3}-K^{-1}]	$\varepsilon'_{\text{pump}}$	$\varepsilon''_{\text{pump}}$
Gold	315	2.13×10^4	2.50×10^6	-24.06	1.51
TiN LQ	28	8.19×10^4	3.13×10^6	-3.63	6.93
TiN HQ	28	8.19×10^4	3.13×10^6	-11.71	4.91

The values of κ, γ, and C_l for gold were taken from [69] and [53]. The values for TiN were taken from [70], [59], and [55]. The permittivites used to calculate the absorption, were taken from experimental data.

A PDEPE system was implemented in Matlab, with the substrate being included as a composite wall. The values used for the substrates are the same as those in Table 5. The temperatures were taken as the values at the front surface. Please refer to [68] for information on setting up a PDEPE solver.

Funding

References

1. R. Boyd, *Nonlinear Optics*, 3rd ed. (Elsevier, 2008).
2. R. L. Sutherland, D. G. Mclean, and S. Kirkpatrick, *Handbook of Nonlinear Optics*, 2nd ed. (Marcel Dekker, 2003).
3. S. A. Maier, *Plasmonics: Fundamentals and Applications* (Springer, 2007).

4. A. A. Maradudin, J. R. Sambles, and W. Barnes, *Modern Plasmonics* (Elsevier, 2014).

5. M. I. Stockman, K. Kneipp, S. I. Bozhevolnyi, S. Saha, A. Dutta, J. Ndukaife, N. Kinsey, H. Reddy, U. Guler, V. M. Shalaev, A. Boltasseva, B. Gholipour, H. N. S. Krishnamoorthy, K. F. MacDonald, C. Soci, N. I. Zheludev, V. Savinov, R. Singh, P. Groß, C. Lienau, M. Vadai, M. L. Solomon, D. R. Barton, M. Lawrence, J. A. Dionne, S. V. Boriskina, R. Esteban, J. Aizpurua, X. Zhang, S. Yang, D. Wang, W. Wang, T. W. Odom, N. Accanto, P. M. de Roque, I. M. Hancu, L. Piatkowski, N. F. van Hulst, and M. F. Kling, "Roadmap on plasmonics," J. Opt. **20**(4), 043001 (2018).

6. M. Mesch, B. Metzger, M. Hentschel, and H. Giessen, "Nonlinear Plasmonic Sensing," Nano Lett. **16**(5), 3155–3159 (2016).

7. K. M. Mayer and J. H. Hafner, "Localized Surface Plasmon Resonance Sensors," Chem. Rev. **111**(6), 3828–3857 (2011).

8. S.-Y. Ding, J. Yi, J.-F. Li, B. Ren, D.-Y. Wu, R. Panneerselvam, and Z.-Q. Tian, "Nanostructure-based plasmon-enhanced Raman spectroscopy for surface analysis of materials," Nat. Rev. Mater. **1**(6), 16021 (2016).

9. J. Lee, M. Tymchenko, C. Argyropoulos, P. Y. Chen, F. Lu, F. Demmerle, G. Boehm, M. C. Amann, A. Alu, and M. A. Belkin, "Giant nonlinear response from plasmonic metasurfaces coupled to intersubband transitions," Nature **511**(7507), 65–69 (2014).

10. D. Traviss, R. Bruck, B. Mills, M. Abb, and O. L. Muskens, "Ultrafast plasmonics using transparent conductive oxide hybrids in the epsilon-near-zero regime," Appl. Phys. Lett. **102**(12), 121112 (2013).

11. C. T. DeVault, V. A. Zenin, A. Pors, K. Chaudhuri, J. Kim, A. Boltasseva, V. M. Shalaev, and S. I. Bozhevolnyi, "Suppression of near-field coupling in plasmonic antennas on epsilon-near-zero substrates," Optica **5**(12), 1557 (2018).

12. S. A. Schulz, A. A. Tahir, M. Z. Alam, J. Upham, I. De Leon, and R. W. Boyd, "Optical response of dipole antennas on an epsilon-near-zero substrate," Phys. Rev. A **93**(6), 063846 (2016).

13. S. Inasawa, M. Sugiyama, and Y. Yamaguchi, "Laser-induced shape transformation of gold nanoparticles below the melting point: The effect of surface melting," J. Phys. Chem. B **109**(8), 3104–3111 (2005).

14. W. Li, U. Guler, N. Kinsey, G. V. Naik, A. Boltasseva, J. Guan, V. M. M. Shalaev, and A. V. Kildishev, "Refractory plasmonics with titanium nitride: broadband metamaterial absorber," Adv. Mater. **26**(47), 7959–7965 (2014).

15. U. Guler, A. Boltasseva, and V. M. Shalaev, "Refractory Plasmonics," Science **344**(6181), 263–264 (2014).

16. M. Kumar, N. Umezawa, S. Ishii, and T. Nagao, "Examining the Performance of Refractory Conductive Ceramics as Plasmonic Materials: A Theoretical Approach," ACS Photonics **3**(1), 43–50 (2016).

17. L. Gui, S. Bagheri, N. Strohfeldt, M. Hentschel, C. M. Zgrabik, B. Metzger, H. Linnenbank, E. L. Hu, and H. Giessen, "Nonlinear Refractory Plasmonics with Titanium Nitride Nanoantennas," Nano Lett. **16**(9), 5708–5713 (2016).

18. M. Kauranen and A. V. Zayats, "Nonlinear Plasmonics," Nat. Photonics **6**(11), 737–748 (2012).

19. S. Lal, S. E. Clare, and N. J. Halas, "Nanoshell-Enabled Photothermal Cancer Therapy: Impending Clinical Impact," Acc. Chem. Res. **41**(12), 1842–1851 (2008).

20. X. Huang, P. K. Jain, I. H. El-Sayed, and M. A. El-Sayed, "Plasmonic photothermal therapy (PPTT) using gold nanoparticles," Lasers Med. Sci. **23**(3), 217–228 (2008).

21. S. Dong, J. Feng, M. Fan, Y. Pi, L. Hu, X. Han, M. Liu, J. Sun, and J. Sun, "Recent developments in heterogeneous photocatalytic water treatment using visible light-responsive photocatalysts: a review," RSC Adv. **5**(19), 14610–14630 (2015).

22. J. Ndukaife, A. Mishra, U. Guler, A. G. A. Nnanna, S. T. Wereley, and A. Boltasseva, "Photothermal heating enabled by plasmonic nanostructures for electrokinetic manipulation and sorting of particles," ACS Nano **8**(9), 9035–9043 (2014).

23. M. L. Juan, M. Righini, and R. Quidant, "Plasmon nano-optical tweezers," Nat. Photonics **5**(6), 349–356 (2011).

24. H. M. L. Robert, F. Kundrat, E. Bermúdez-Ureña, H. Rigneault, S. Monneret, R. Quidant, J. Polleux, and G. Baffou, "Light-Assisted Solvothermal Chemistry Using Plasmonic Nanoparticles," ACS Omega **1**(1), 2–8 (2016).

25. A. A. Golubev, B. N. Khlebtsov, R. D. Rodriguez, Y. Chen, and D. R. T. Zahn, "Plasmonic Heating Plays a Dominant Role in the Plasmon-Induced Photocatalytic Reduction of 4-Nitrobenzenethiol," J. Phys. Chem. C **122**(10), 5657–5663 (2018).

26. S. Ishii, S. L. Shinde, W. Jevasuwan, N. Fukata, and T. Nagao, "Hot Electron Excitation from Titanium Nitride Using Visible Light," ACS Photonics **3**(9), 1552–1557 (2016).

27. H. Xia, X. Wen, Y. Feng, R. Patterson, S. Chung, N. Gupta, S. Shrestha, and G. Conibeer, "Hot carrier dynamics in HfN and ZrN measured by transient absorption spectroscopy," Sol. Energy Mater. Sol. Cells **150**, 51–56 (2016).

28. U. Guler, J. C. Ndukaife, G. V Naik, A. G. A. Nnanna, A. V Kildishev, V. M. Shalaev, and A. Boltasseva, "Local Heating with Lithographically Fabricated Plasmonic Titanium Nitride Nanoparticles," (2013).

29. R. W. Boyd, Z. Shi, and I. De Leon, "The third-order nonlinear susceptibility of gold," Opt. Commun. **326**, 74–79 (2014).

30. N. Bloembergen, W. K. Burns, and M. Matsuoka, "Reflected third harmonic generated by picosecond laser pulses," Opt. Commun. **1**(1), 1–2 (1969).

31. A. Capretti, Y. Wang, N. Engheta, and L. Dal Negro, "Near-Zero Indium Tin Oxide and Titanium Nitride Nanolayers Excited in the Near-InfraredSpectral Range," ACS Photonics **2**(11), 1584–1591 (2015).

32. N. Kinsey, A. A. Syed, D. Courtwright, C. DeVault, C. E. Bonner, V. I. Gavrilenko, V. M. Shalaev, D. J. Hagan, E. W. Van Stryland, and A. Boltasseva, "Effective third-order nonlinearities in metallic refractory titanium nitride thin films," Opt. Mater. Express **5**(11), 2395–2403 (2015).

33. B. Doiron, Y. Li, A. P. Mihai, L. F. Cohen, P. K. Petrov, N. M. Alford, R. F. Oulton, and S. A. Maier, "Comparison of the ultrafast hot electron dynamics of titanium nitride and gold for plasmonic applications," in *Proc. SPIE*, T. Tanaka and D. P. Tsai, eds. (SPIE, 2017), p. 3.

34. B. Doiron, Y. Li, A. Mihai, S. D. Forno, S. Fearn, L. F. Cohen, N. M. Alford, J. Lischner, P. Petrov, S. A. Maier, and R. F. Oulton, "Optimizing hot electron harvesting at planar metal-semiconductor interfaces with titanium oxynitride thin films," ArXiv:1807.03702 (2018).

35. N. Kinsey, M. Ferrera, G. V. Naik, V. E. Babicheva, V. M. Shalaev, and A. Boltasseva, "Experimental demonstration of titanium nitride plasmonic interconnects," Opt. Express **22**(10), 12238–12247 (2014).

36. D. Shah, H. Reddy, N. Kinsey, V. M. Shalaev, and A. Boltasseva, "Optical Properties of Plasmonic Ultrathin TiN Films," Adv. Opt. Mater. **5**(13), 1700065 (2017).

37. M. R. Ferdinandus, H. Hu, M. Reichert, D. J. Hagan, and E. W. Van Stryland, "Beam deflection measurement of time and polarization resolved ultrafast nonlinear refraction," Opt. Lett. **38**(18), 3518–3521 (2013).

38. M. R. Ferdinandus, J. M. Reed, K. L. Averett, F. K. Hopkins, and A. Urbas, "Analysis of beam deflection measurements in the presence of linear absorption," Opt. Mater. Express **7**(5), 1598 (2017).

39. E. Xenogiannopoulou and P. Aloukos, "Third-order nonlinear optical properties of thin sputtered gold films," Opt. Commun. **275**(1), 217–222 (2007).

40. D. D. Smith, Y. Yoon, R. W. Boyd, J. K. Campbell, L. A. Baker, R. M. Crooks, and M. George, "Z-Scan Measurement of the Nonlinear Absorption of a Thin Gold Film," J. Appl. Phys. **86**(11), 6200–6205 (1999).

41. D. C. Hutchings, M. Sheik-Bahae, D. J. Hagan, and E. W. Van Stryland, "Kramers-Kronig relations in nonlinear optics," Opt. Quantum Electron. **24**(1), 1–30 (1992).

42. M. Marlo and V. Milman, "Density-functional study of bulk and surface properties of titanium nitride using different exchange-correlation functionals," Phys. Rev. B **62**(4), 2899–2907 (2000).

43. M. Kumar, S. Ishii, N. Umezawa, and T. Nagao, "Band engineering of ternary metal nitride system Ti1-x ZrxN for plasmonic applications," Opt. Mater. Express **6**(1), 29 (2016).

44. P. M. Norris, A. P. Caffrey, R. J. Stevens, J. M. Klopf, J. T. McLeskey, and A. N. Smith, "Femtosecond pump-probe nondestructive examination of materials (invited)," Rev. Sci. Instrum. **74**(1), 400–406 (2003).

45. C.-K. Sun, F. Vallée, S. Keller, J. E. Bowers, and S. P. DenBaars, "Femtosecond studies of carrier dynamics in InGaN," Appl. Phys. Lett. **70**(15), 2004–2006 (1997).

46. C.-K. Sun, F. Vallée, L. H. Acioli, E. P. Ippen, and J. G. Fujimoto, "Femtosecond-tunable measurement of electron thermalization in gold," Phys. Rev. B **50**(20), 15337–15348 (1994).

47. H. Elsayed-Ali, T. Norris, M. Pessot, and G. Mourou, "Time-resolved observation of electron-phonon relaxation in copper," Phys. Rev. Lett. **58**(12), 1212–1215 (1987).

48. J. Hohlfeld, S. S. Wellershoof, J. Güdde, U. Conrad, V. Jähnke, and E. Matthias, "Electron and lattice dynamics following optical excitation of metals," Chem. Phys. **251**(1-3), 237–258 (2000).

49. S. I. Anisimov, B. L. Kapeliovich, and T. L. Perel'man, "Electron emission from metal surfaces exposed to ultrashort laser pulses," JETP **39**, 375 (1974).

50. Y. Zhang, D. Y. Tzou, and J. K. Chen, "Micro- and Nanoscale Heat Transfer in Femtosecond Laser Processing of Metals," in *High-Power and Femtosecond Lasers: Properties, Materials and Applications*, P. H. Barret and M. Palmerm, eds. (Nova Science Publishers, 2009), pp. 159–206.

51. P. G. Klemens and R. K. Williams, "Thermal conductivity of metals and alloys," Int. Mater. Rev. **31**(1), 197–215 (1986).

52. S. D. Brorson, A. Kazeroonian, J. S. Moodera, D. W. Face, T. K. Cheng, E. P. Ippen, M. S. Dresselhaus, and G. Dresselhaus, "Femtosecond room-temperature measurement of the electron-phonon coupling constant in metallic superconductors," Phys. Rev. Lett. **64**(18), 2172–2175 (1990).

53. P. B. Allen, "Theory of thermal relaxation of electrons in metals," Phys. Rev. Lett. **59**(13), 1460–1463 (1987).

54. L. Guo and X. Xu, "Ultrafast Spectroscopy of Electron-Phonon Coupling in Gold," J. Heat Transfer **136**(12), 122401 (2014).

55. R. M. Costescu, M. A. Wall, and D. G. Cahill, "Thermal conductance of epitaxial interfaces," Phys. Rev. B **67**(5), 054302 (2003).

56. P. Patsalas, N. Kalfagiannis, and S. Kassavetis, "Optical Properties and Plasmonic Performance of Titanium Nitride," Materials **8**(6), 3128–3154 (2015).

57. M. Reichert, H. Hu, M. R. Ferdinandus, M. Seidel, P. Zhao, T. R. Ensley, D. Peceli, J. M. Reed, D. A. Fishman, S. Webster, D. J. Hagan, and E. W. Van Stryland, "Temporal, spectral, and polarization dependence of the nonlinear optical response of carbon disulfide," Optica **1**(6), 436 (2014).

58. P. Roedhammer, W. Weber, E. Gmelin, and K. H. Rieder, "Low temperature specific heat and phonon anomalies in transition metal compounds," 581, (1976).

59. V. A. Lovchinov, H. Mädge, and N. A. Christensen, "Low Temperature Specific Heat of TiNx," Phys. Scr. **25**(5), 649–650 (1982).

60. B. Altintas, "On the high pressure superconductivity of transition metal nitride: TiN," Phys. C Supercond. **487**, 37–41 (2013).

61. S. K. Gupta, S. D. Gupta, H. R. Soni, V. Mankad, and P. K. Jha, "First-principles studies of the superconductivity and vibrational properties of transition-metal nitrides TMN (TM = Ti, V, and Cr)," Mater. Chem. Phys. **143**(2), 503–513 (2014).

62. E. I. Isaev, S. I. Simak, I. A. Abrikosov, R. Ahuja, Y. K. Vekilov, M. I. Katsnelson, and A. I. Lichtenstein, "Phonon related properties of transition metals, their carbides, and nitrides: A first- principles study," J. Appl. Phys. **101**(12), 123519 (2007).
63. W. Spengler, R. Kaiser, A. N. Christensen, and G. Muller-Vogt, "Raman scattering, superconductivity, and phonon density of states of stoichiometric and nonstoichiometric TiN," Phys. Rev. B **17**(3), 1095–1101 (1978).
64. H. Reddy, U. Guler, Z. Kudyshev, A. V. Kildishev, V. M. Shalaev, and A. Boltasseva, "Temperature-Dependent Optical Properties of Plasmonic Titanium Nitride Thin Films," ACS Photonics **4**(6), 1413–1420 (2017).
65. J. F. Shackelford and W. Alexander, *CRC Materials Science and Engineering Handbook* (CRC Press, 2001).
66. R. Lide, *CRC Handbook of Chemistry and Physics*, 86th ed. (CRC Press, 2005).
67. B. F. Naylor, "High-temperature heat contents of Titanium Carbide and Titanium Nitride," J. Am. Chem. Soc. **68**(3), 370–371 (1946).
68. P. Howard, "Partial Differential Equations in MATLAB 7 . 0 PDE in One Space Dimension," 1, 1–23 (2005).
69. P. B. Johnson and R. W. Christy, "Optical Constants of the Noble Metals," Phys. Rev. B **6**(12), 4370–4379 (1972).
70. J. Shackelford, Y.-H. Han, S. Kim, and S.-H. Kwon, *Materials Science and Engineering Handbook* (CRC Press, 2015).